Ultrathin $WO_3 \cdot 0.33H_2O$ Nanotubes for CO_2 Photoreduction to Acetate with High Selectivity

Songmei Sun,*,† Motonori Watanabe,† Ji Wu,† Qi An,‡ and Tatsumi Ishihara*,†

†International Institute for Carbon-Neutral Energy Research (I2CNER), Kyushu University, Fukuoka 819-0395, Japan

‡Department of Chemical and Materials Engineering, University of Nevada, Reno, Nevada 89557-0388, United States

* Supporting Information

ABSTRACT: Artificial photosynthesis from CO_2 reduction is severely hampered by the kinetically challenging multi-electron reaction process. Oxygen vacancies (Vo) with abundant localized electrons have great potential to overcome this limitation. However, surface Vo usually have low concentrations and are easily oxidized, causing them to lose their activities. For practical application of CO_2 photoreduction, fabricating and enhancing the stability of Vo on semiconductors is indispensable. Here we report the first synthesis of ultrathin $WO_3 \cdot 0.33H_2O$ nanotubes with a large amount of exposed surface Vo sites, which can realize excellent and stable CO_2 photoreduction to CH_3COOH in pure water under solar light. The selectivity for acetum generation is up to 85%, with an average productivity of about 9.4 μmol g^{-1} h^{-1}. More importantly, Vo in the catalyst are sustainable, and their concentration was not decreased even after 60 h of reaction. Quantum chemical calculations and in situ DRIFT studies revealed that the main reaction pathway might be $CO_2 \rightarrow {}^{\bullet}COOH \rightarrow (COOH)_2 \rightarrow CH_3COOH$.

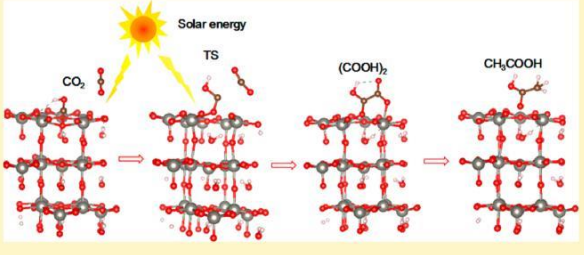

INTRODUCTION

Artificial photosynthesis from CO_2 reduction has attracted particular interest because of its dual effects on both suppressing the greenhouse effect and alleviating society's dependence on fossil fuels.[1−7] However, the conversion of CO_2 requires high energy input because of the high dissociation energy of the C O bond (~750 kJ/mol).[8] Therefore, most of the catalysts studied for photochemical CO_2 reduction were wide band gap semiconductors which could provide enough negative electrons for CO_2 reduction but only respond under UV light, such as TiO_2,[9−12] $SrTiO_3$,[13] ZnS,[14,15] Zn_2GeO_4,[16] $InTaO_4$,[17] etc. In addition, H_2 evolution usually competes with the CO_2 reduction because H^+ reduction is kinetically more favorable,[18] severely decreasing the selectivity for CO_2 reduction.

To overcome the above-mentioned limitations, a desirable photocatalyst should have a broad solar light absorption along with a highly active and selective CO_2 reduction performance. Among the various semiconductor photocatalysts, tungsten trioxide (WO_3), with a small band gap of 2.4−2.8 eV, has been demonstrated as one of the most promising candidates because of its strong solar light adsorption, stable physicochemical properties, and relatively low conduction band edge potential for suppressing H^+ reduction.[19−21] However, the low conduction band potential also suppresses the CO_2 reduction performance because the reduction power of the photogenerated electrons is insufficient. Up to the present, only C_1 products (such as CH_4, CH_3OH) were obtained from CO_2 photoreduction with a reaction rate lower than 2.5 μmol/g·h.[22−24] Elevating the conduction band edge and increasing the CO_2 activation on the WO_3 surface are indispensable to significantly improve its photocatalytic activity.

Construction of an atomic-scale nanostructure provides a unique opportunity to improve both the conduction band potential and CO_2 activation by modifying the particle size and surface microstructure of the photocatalyst. For instance, quantum-sized semiconductors have been proved to possess an elevated conduction band and exhibit much improved performance for water splitting.[25−28] In addition, when the particle size decreases to quantum size, the extremely large fraction of low-coordinated surface atoms will largely improve the molecular adsorption.[5,29] A recent study by Zeng et al. reported that the surface negative charge density generally determines the adsorption and activation of CO_2.[30,31] At present, the general approach for improving the surface negative charge density involves loading noble metals to improve the performance of photocatalytic CO_2 reduction.[9,32,33] However, for metal oxide semiconductors, constructing surface oxygen vacancies (Vo) may be a more economical and accessible approach for increasing surface negative charge density, since the positively charged Vo can accumulate excess free electrons during the photocatalysis and play a role similar to that of noble metals.[34,35] Several studies have been reported on the application of Vo in photocatalytic CO_2 reduction,[10,22,36,37] proving the feasibility of this approach. However, it was found that the Vo is not stable, and only C_1 product was obtained with these catalysts. Importantly, a design

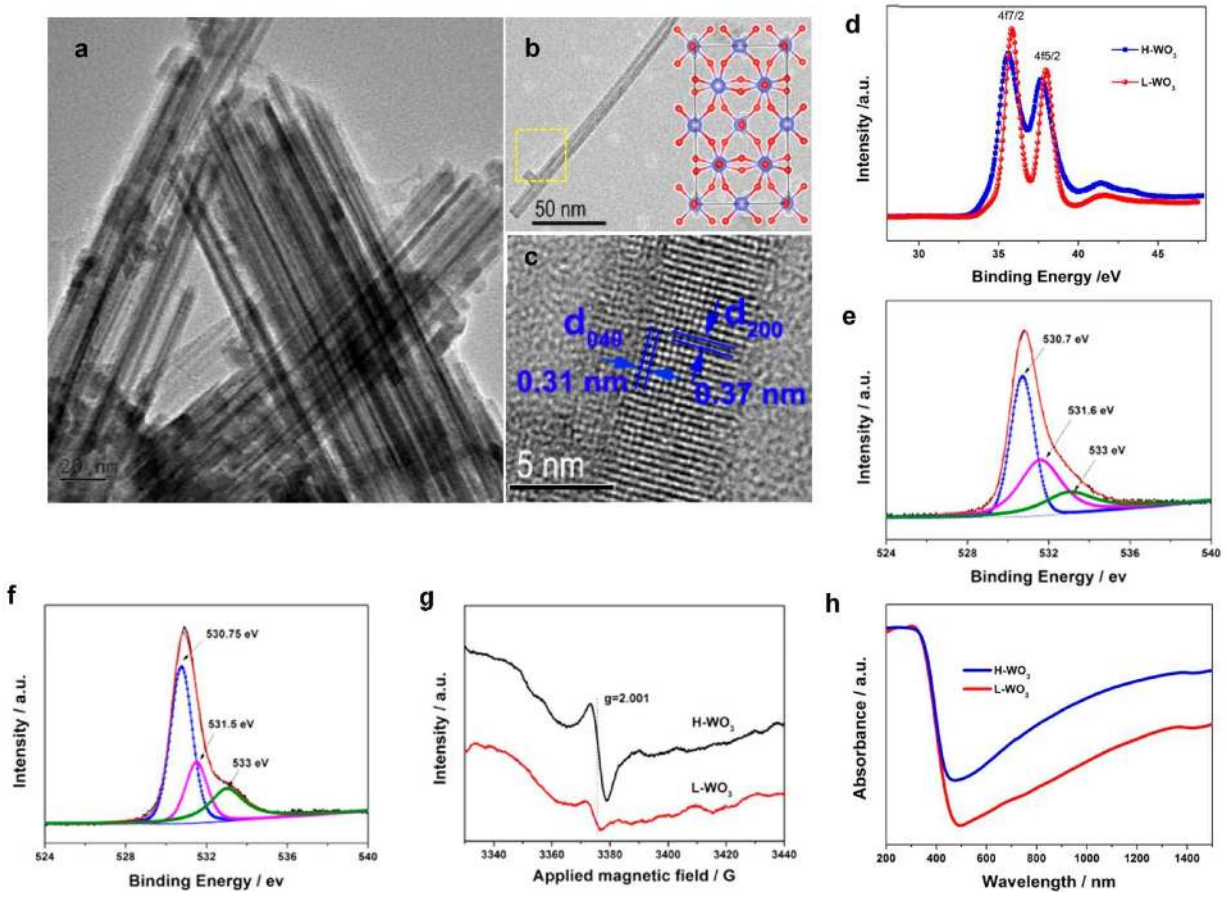

Figure 1. Characterization of the hydrothermally synthesized H-WO_3 sample. (a) Low-magnification TEM image of the H-WO_3 nanotube sample. (b) High-magnification TEM image of one single nanotube. Inset: Schematic atomic model of $WO_3 \cdot 033H_2O$ (Fmm2), clearly showing the atomic configuration of W/O along the [001] direction: red, oxygen; blue, tungsten; gray, hydrogen. (c) HRTEM image of the nanotube from the area marked with the yellow box in (b). (d) W 4f XPS spectrum of the as-prepared $WO_3 \cdot 033H_2O$ sample. (e) O 1s XPS spectrum of the H-WO_3 sample. (f) O 1s XPS spectrum of the L-WO_3 sample. (g) ESR spectra of different $WO_3 \cdot 0.33H_2O$ samples at 300 K in N_2. (h) Ultraviolet−visible−near-infrared absorption spectrum of the oxygen-deficient $WO_3 \cdot 033H_2O$ samples.

principle for stable and sustainable Vo-functional photocatalyst has not been established yet.

In this work, we report a new $WO_3 \cdot 0.33H_2O$ catalyst with a large amount of sustainable surface Vo sites for highly efficient CO_2 reduction to CH_3COOH under solar light. CH_3COOH is found to be the main product, with a high selectivity >80% from CO_2 photoreduction. Computational and experimental results proved that Vo active sites can be sustainably used because of a unique C−C bond formation process.

RESULTS AND DISCUSSION

Quantum sized $WO_3 \cdot 0.33H_2O$ with high concentration of Vo (H-WO_3) was synthesized by an oleate-assisted hydrothermal synthesis method. The XRD pattern (Figure S1) of the H-WO_3 sample can be indexed to orthorhombic $WO_3 \cdot 0.33H_2O$ (JCPDS card no. 87-1203). Transmission electron microscopy (TEM) images (Figure 1a,b) indicate an ultrathin tube-like structure with a uniform diameter of ~8 nm and a wall thickness of ~2 nm. The surface structure of the nanotube was further observed by high-resolution TEM (HRTEM) imaging of the area marked in Figure 1b. As shown in Figure 1c, the lattice spacing along the growth orientation of the nanotube was measured to be 0.37 nm, which corresponds to the d spacing of the {200} plane. The {040} lattice plane was also clearly observed, with a d spacing of 0.31 nm. Both the {200} and {040} planes belong to the [001] zone axis, indicating that the surface plane of the $WO_3 \cdot 0.33H_2O$ nanotube is the {001} plane. A schematic of the crystal structure of $WO_3 \cdot 0.33H_2O$ along the [001] direction in the inset of Figure 1b displays the same orientation and arrangement of the {040} and {200} planes as that observed from Figure 1c. Oleate ions played an important role in the formation of this ultrathin nanotube structure (detailed illustration shown in Figure S2). For comparison, a $WO_3 \cdot 0.33H_2O$ (L-WO_3) sample with similar grain size (Figures S1 and S3) but lower Vo concentrations was also prepared under the same conditions without added oleate ions.

High-resolution X-ray photoelectron spectroscopy (XPS) revealed the surface chemical environment of the as-prepared $WO_3 \cdot 0.33H_2O$ samples. Compared with the L-WO_3 sample, the W 4f7/2 and W 4f5/2 peaks of the H-WO_3 sample (Figure 1d) are decreased from 35.85 and 37.95 eV to 35.6 and 37.65 eV, respectively, indicating a lower valence state of W in the H-WO_3 sample, which possesses higher Vo concentration. The surface Vo concentration was estimated from the high-resolution O 1s XPS spectrum. As shown in Figure 1e, the peak at 530.7 eV is ascribed to the lattice oxygen, while the other two peaks located at 531.6 and 533 eV are attributed to the O-atoms in the vicinity of Vo and the O-atoms in the surface OH, respectively. The relative concentration of the

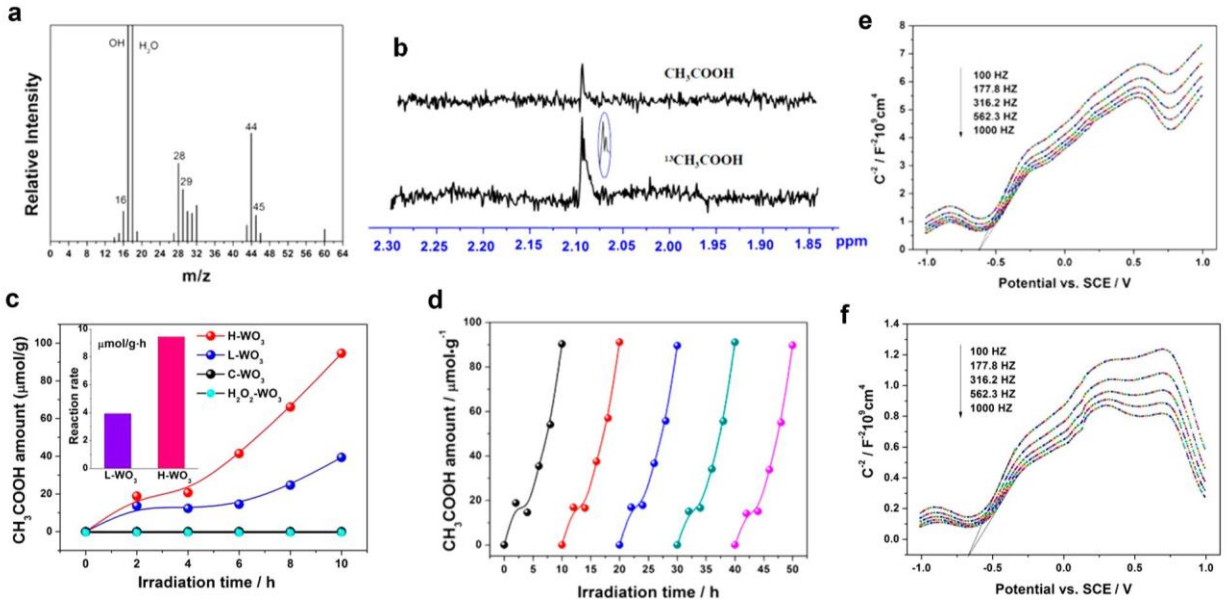

Figure 2. Photocatalytic CO_2 reduction performance of the as-prepared oxygen-deficient $WO_3 \cdot 033H_2O$ samples under simulated solar light irradiation. (a) Mass spectra extracted from GC-MS analysis of acetic acid product from $^{13}CO_2$ reduction on hydrated H-WO_3 sample in water. (b) ^1H NMR spectra of the obtained acetum product in D_2O-saturated water solution by using different $^{12}CO_2$ and $^{13}CO_2$ gas on H-WO_3 catalyst. (c) Acetum evolution along with irradiation times in pure water. Inset: acetum formation rate of the different samples. (d) Photostability of the as-prepared hydrated H-WO_3 sample for CO_2 reduction under simulated solar light irradiation. (e) Mott−Schottky plot of the as-prepared H-WO_3 electrode in 0.1 M Na_2SO_4. (f) Mott−Schottky plot of the as-prepared L-WO_3 electrode in 0.1 M Na_2SO_4.

surface O-atoms around Vo can be calculated to be about 36.4% (Figure 1e) in the H-WO_3 sample. The L-WO_3 sample possesses much lower surface O-atoms around Vo, with their concentration calculated to be about 22.3% (Figure 1f).

The presence of Vo was also evidenced by electron spin resonance (ESR) imaging (Figure 1g). A characteristic single-electron-trapped Vo signal with a g-factor of 2.001 was observed for the H-WO_3 and L-WO_3 samples at room temperature in N_2 gas. The higher Vo concentration in the H-WO_3 sample was also observed from the ultraviolet−visible−near-infrared absorption spectrum (Figure 1h). Because of the similar grain size, the intrinsic UV−vis absorption edges of the two different $WO_3 \cdot 0.33H_2O$ samples are almost the same, generating a similar intrinsic band gap of about 2.85 eV. However, a higher broad absorption tail appeared in the H-WO_3 sample. A density functional theory (DFT) calculation on the band structure (Figure S4) proved that this absorption tail comes from a Vo-associated middle band in the band gap of oxygen-deficient $WO_3 \cdot 0.33H_2O$ sample.

To assess the catalytic performance, photocatalytic CO_2 reduction was performed in pure water under a solar light simulator. Before the CO_2 reduction, the catalyst powder was dispersed into 100 mL of water and then irradiated under a 300 W Xe lamp for 6 h to eliminate any surface organic contaminants during the catalyst preparation process. Solid-state ^{13}C NMR (Figure S5) confirmed that the surface organic contaminants were eliminated by this photocatalytic oxidation process. We also conducted a control experiment by Ar bubbling. It was found that there was no organic substance in the reaction solution before and after light irradiation. After that, the $WO_3 \cdot 0.33H_2O$ catalyst was used for the photocatalytic CO_2 reduction reaction. It was found that the main product of CO_2 reduction on the as-prepared $WO_3 \cdot 0.33H_2O$ samples was CH_3COOH under simulated solar light irradiation, while small amounts of HCOOH and CO were also detected. H_2, as the most-reported competing product, exhibited only trace amounts in this experiment, indicating the high selectivity of the photocatalyst for CO_2 reduction. Before a quantitative evaluation of the catalytic performance, control experiments showed that CH_3COOH, CO, and HCOOH could not be detected by gas chromatography and ion chromatography in the absence of the catalyst or in the dark, indicating that the product comes from photocatalytic reaction. To further prove the CO_2 reduction, isotopic $^{13}CO_2$ gas was used as the reactant, and the liquid products obtained after 4 h irradiation were identified by GC-MS and NMR. In the mass spectrum extracted from GC-MS analysis (Figure 2a), the molecular ion peak appeared at an m/z value of 60, which can be ascribed to the ionic CH_3COO^- with one carbon labeled. According to the standard fragmentation pattern of acetic acid, the highest peak appeared at m/z 43 (Figure S6), corresponding to the fragmented CH_3CO. In the ^{13}C-labeled acetic hydrate product, the highest peak appeared at m/z 44 instead of 43. The m/z peak of fragmented CH_3 also shifted from 15 to 16, proving the presence of ^{13}C species in the CH_3 fragment. The non-isotope-labeled $^{12}COOH$ fragment comes from the tightly adsorbed surface HCO_3 species (further proved by TPD, DRIFT, and DFT calculation in the following section) which could not eliminated by Ar bubbling. ^1H NMR spectroscopy was also used to detect the ^{13}C species in the obtained acetum product. As shown in Figure 2b, if $^{12}CO_2$ was used as the carbon source, only a singlet was observed around 2.07 ppm, which is the characteristic methyl proton peak for CH_3COOH in D_2O. However, if the carbon source was changed to $^{13}CO_2$ gas, the methyl proton resonance at δ 2.07 was split into two peaks, due to a one-bond coupling between ^{13}C and ^1H. These studies clearly show that the CH_3COOH product indeed comes from CO_2 reduction.

Figure 2c summarizes the photocatalytic CO_2 reduction activity of the as-prepared $WO_3 \cdot 0.33H_2O$ samples. As shown in

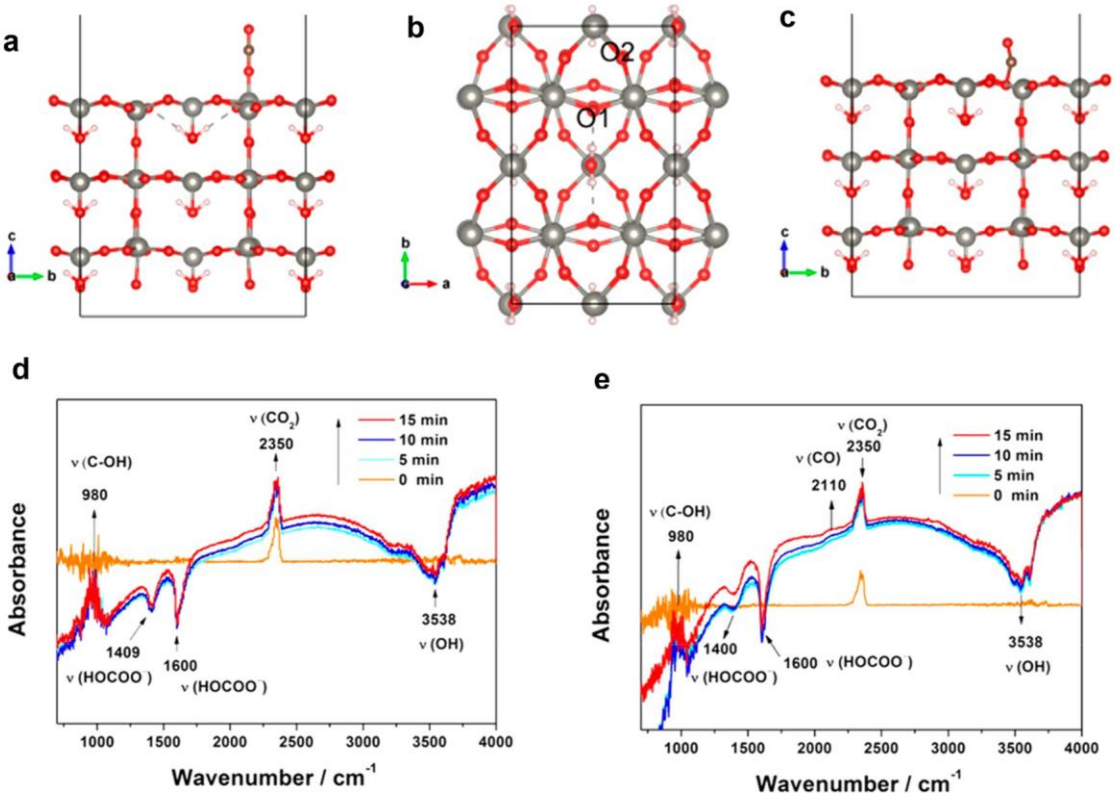

Figure 3. CO_2 adsorption and activation on different $WO_3 \cdot 0.33H_2O$ samples revealed by DFT calculation (a−c) and in situ DRIFT observations (d,e). (a) CO_2 adsorption on a perfect {001} surface. (b) Possible Vo sites on the {001} surface. (c) CO_2 adsorption on an oxygen-deficient $WO_3 \cdot 0.33H_2O$ {001} surface (red, oxygen; gray, tungsten; white, hydrogen; sienna, carbon). (d) In situ DRIFT spectrum of the H-WO_3 sample after ambient temperature adsorption of CO_2 under solar light irradiation. (e) In situ DRIFT spectrum of the L-WO_3 sample after ambient temperature adsorption of CO_2 under solar light irradiation.

Figure 2c, the acetum yield gradually increased with the photocatalytic time, and the total yield of acetum obtained by the H-WO_3 sample was about 94 μmol/g after 10 h, corresponding to an CH_3COOH generation rate of 9.4 μmol/g·h (Figure 2c). The flat stage for acetum generation before 4 h may be ascribed to the low concentration of the dissolved CO_2 (HCO_3^-) initially. After the surface pre-adsorbed HCO_3 species (proved by in situ DRIFT in the following section) is transformed into the final product, the acetate generation rate may depend on the HCO_3^- concentration in the reaction solution. This phenomenon has been observed in electrochemical CO_2 reduction experiments.[38] For the H-WO_3 sample, the HCO_3^- concentration can be largely increased only under light irradiation. An obvious HCO_3^- peak at δ 160.4 was observed in the ^{13}C NMR spectrum after 5 h irradiation (Figure S7), and this peak rapidly increased along with the irradiation time. Without light irradiation, there is no peak observed in the ^{13}C NMR spectrum within 5 h. This finding demonstrates that HCO_3^- may be an important intermediate for acetum generation by the H-WO_3 catalyst. There is no O_2 evolved in the reaction system during the CO_2 reduction experiment. After photocatalytic reaction for 10 h, a total amount of 17.6 μmol of H_2O_2 was detected by the titanium sulfate spectrophotometric method in the reaction solution, indicating that H_2O provides the protons for acetum generation.

Besides the acetum product, small amounts of CO and formic acid were also detected in the reaction system. After 10 h, the total amounts of CO (Figure S8a) and HCOOH (Figure S8b) produced by H-WO_3 catalyst were 1.12 and 15 μmol/g, respectively, indicating the high selectivity (85%) for acetum production. The L-WO_3 sample with lower Vo concentration exhibits an obvious decreased activity for CH_3COOH production but a much increased CO production when compared with the H-WO_3 sample (Figure S8). The higher photocatalytic activity of L-WO_3 sample for CO production is ascribed to its higher conduction band potential (discussed in detail in the following section).

To further confirm the important role of Vo for the CH_3COOH production, the H-WO_3 sample was oxidized with 30% hydrogen peroxide (H_2O_2) for 5 h to eliminate the surface Vo. The color of the sample changed from medium blue to light yellow. The experiment on CO_2 reduction by the H_2O_2-treated H-WO_3 (H_2O_2-WO_3) sample indicates that there was no acetum generated in the final reaction solution, similar to the performance of commercial WO_3 (C-WO_3).

To evaluate the photocatalytic stability of the as-prepared H-WO_3 sample, the used catalysts were re-collected, washed, and freeze-dried for recycling tests. As demonstrated in Figure 2d, after six consecutive runs (60 h), the photocatalytic activity of the H-WO_3 nanotube for acetum production was well-maintained. The total amount of acetum obtained was 562 μmol/g within 60 h, which is equivalent to a turnover number of 1.07 for the consumed photogenerated electrons for acetum generation. This suggests that acetum evolution under these conditions is catalytic. The X-ray diffraction (XRD) pattern (Figure S9) of the spent H-WO_3 is almost the same as that of the initial sample. In addition, XPS analysis (Figure S10)

revealed that the relative concentration of the surface O-atoms around Vo was also well maintained (38%) after photocatalytic reaction, further proving the high stability of Vo.

To investigate the thermodynamic feasibility of the as-prepared $WO_3 \cdot 0.33H_2O$ samples for acetum generation, the conduction band potential of the catalysts was studied by electrochemical measurements. Figure 2e,f shows the Mott−Schottky spectrum of the as-prepared $WO_3 \cdot 0.33H_2O$ samples, which is usually used for analysis of the flat band potential (E_{fb}) of semiconductor electrodes.[39] The E_{fb} values calculated from the intercept of the axis with potential values were −0.62 and −0.67 V vs SCE for H-WO_3 and L-WO_3, respectively. For many n-type semiconductors, E_{fb} is considered to be about 0.1 V below the conduction band (E_{cb}).[40] Based on this, the estimated E_{cb} values of the H-WO_3 and L-WO_3 samples were −0.48 and −0.53 V vs NHE at pH 7. Although the E_{cb} value decreased in H-WO_3 along with increasing Vo concentration, the photogenerated electrons in the H-WO_3 sample still have enough energy to reduce CO_2 to acetum, because the CO_2/CH_3COO^- redox potential (−0.29 V vs NHE at pH 7) is much lower than the E_{cb} value of the catalyst. Besides E_{cb}, the conductivity of the H-WO_3 sample was found to be slightly decreased because of the increased Vo concentration when compared with the L-WO_3 sample (Figure S11). Although both the decreased E_{cb} and the conductivity may lower the CO_2 reduction activity, the H-WO_3 sample still exhibits a much improved photocatalytic performance, which may be ascribed to its higher Vo concentration and the larger BET surface area of the nanotube structure.

An interesting question raised in the experiment is why the as-prepared $WO_3 \cdot 0.33H_2O$ samples exhibited highly efficient and sustainable photocatalytic activity for acetum production, which is an eight-electron-transfer reduction process. Kinetically, CO is the most likely product from CO_2 reduction because this process needs only two electrons. However, this process is thermodynamically difficult, because the redox potential of CO_2/CO is as high as −0.53 V vs NHE at pH 7. From the electrochemical measurement, the conduction band electrons of the as-prepared $WO_3 \cdot 0.33H_2O$ samples do not have enough energy for efficient CO_2 reduction to CO. A multi-electron reduction process, which possesses a relatively low thermodynamic barrier, is more possible with these $WO_3 \cdot 0.33H_2O$ catalysts. For multi-electron reduction, an activation process is necessary to promote the reaction rate.

To investigate the CO_2 activation, quantum chemical calculations were conducted to explore the adsorption property of CO_2 on the surface of $WO_3 \cdot 0.33H_2O$. For the defect-free surface, we expected that the CO_2 will be on top of the surface W atoms, as shown in Figure 3a. The calculated binding energy is 0.08 eV, and the C O bond length is increased only from 1.169 to 1.177 Å, suggesting a weak activation of CO_2 by the perfect {001} surface. For the oxygen-deficient {001} surface, there are two possible Vo sites, as shown in Figure 3b. The O1 site has the longer O−W bond distance (1.972 Å) of these two sites, suggesting it is the more plausible Vo site. Thus, we removed the O-atom in the O1 site and added one CO_2 molecule to this site. The calculated binding energy of CO_2 on the O1 site is 1.32 eV, much larger than that on the defect-free surface. The energetically stable configurations of CO_2 are shown in Figure 3c. It was found that the C O bond close to the Vo was lengthened from 1.169 to 1.4589 Å, which is similar to the single C−O bond length, indicating the potential advantage of an oxygen-deficient surface for CO_2 activation.

To further investigate the role of Vo on the adsorption and activation of CO_2, an in situ diffuse reflectance Fourier transform infrared spectroscopy (DRIFT) study was performed on the as-prepared catalysts. Before introducing CO_2, we analyzed the DRIFT spectrum of the $WO_3 \cdot 0.33H_2O$ catalyst under a vacuum in the dark (Figure S12). The H-WO_3 surface was dominated by strongly adsorbed OH and CO_2 in the vacuum state. The absorption bands at ~1420−1620 cm^{-1} are ascribed to the symmetric and asymmetric OCO stretching vibrations of the surface bicarbonate HCO_3 species, which is formed by interaction of Vo-adsorbed CO_2 with surface hydroxyl.[9,41] The small absorption bands around ~1550 cm^{-1} are bidentate or monodentate carbonate species (b-CO_3^{2-}, m-CO_3^{2-}).[42,43] The strong absorption bands around 3538 cm^{-1} are attributed to the stretching vibration of the surface W−OH groups. Another strong absorption band around 2350 cm^{-1} is ascribed to the asymmetric stretching vibration of linear adsorbed CO_2.

In situ DRIFT spectra of CO_2 with H_2O vapor during photoirradiation were further recorded for studying the adsorption and activation processes. The DRIFT absorption spectra were obtained by subtracting the $WO_3 \cdot 0.33H_2O$ background in a vacuum. Both the H-WO_3 and L-WO_3 exhibited similar behaviors in the DRIFT under light irradiation. As shown in Figure 3d,e, after introduction of CO_2, a distinct linearly absorbed CO_2 was observed at ~2350 cm^{-1}. In situ solar light irradiation of the H-WO_3 sample for 5 min resulted in the appearance of three obvious negative absorption bands at ~1400, 1600, and 3540 cm^{-1}, along with a new positive absorption peak at ~980 cm^{-1}. The negative absorption bands at ~1400 and 1600 cm^{-1} are assigned to the decreased concentration of surface bicarbonate under light irradiation. Besides, it was found the absorption bands of bicarbonate species are red-shifted by −20 cm^{-1}, indicating the HCO_3 species further adsorbed on the catalyst surface after light irradiation, which is consistent with the theoretical simulation result which will be discussed in the following section. The negative absorption band around 3540 cm^{-1} is related to the decrease of surface hydroxyl OH. The positive absorption band that appears around 980 cm^{-1} is most probably the C−O stretching band of the newly formed C− OH from surface HCO_3 reduction. There is no decrease in the absorption band for bidentate or monodentate carbonate, indicating that these CO_3^{2-} species are not active for further photoreduction. From the above, the in situ DRIFT study suggests a reaction between the surface bicarbonate species and hydroxyl to produce the COOH intermediate, which has been proved to be the kinetically dominant key intermediate leading to CO_2 reduction.[44,45]

CO_2 temperature-programmed desorption (TPD) profiles of the H-WO_3 and L-WO_3 samples are provided in Figure S13. Based on the above DRIFT data, the TPD profiles were deconvoluted into four desorption peaks: a low-temperature peak at 66 °C, assigned to the linear adsorbed CO_2 by surface OH; middle-temperature peaks around 280 and 320 °C, attributed to bidentate or monodentate carbonate species (b-CO_3^{2-}, m-CO_3^{2-}); and a high-temperature peak after 350 °C, assigned to CO_2 desorption from Vo.[46] From the TPD spectrum, it was found that the H-WO_3 sample has much higher Vo-adsorbed CO_2 but lower linear adsorbed CO_2 than the L-WO_3 sample, further proving that the improvement in CH_3COOH generation in the H-WO_3 sample is closely related to the higher Vo-adsorbed bicarbonate species.

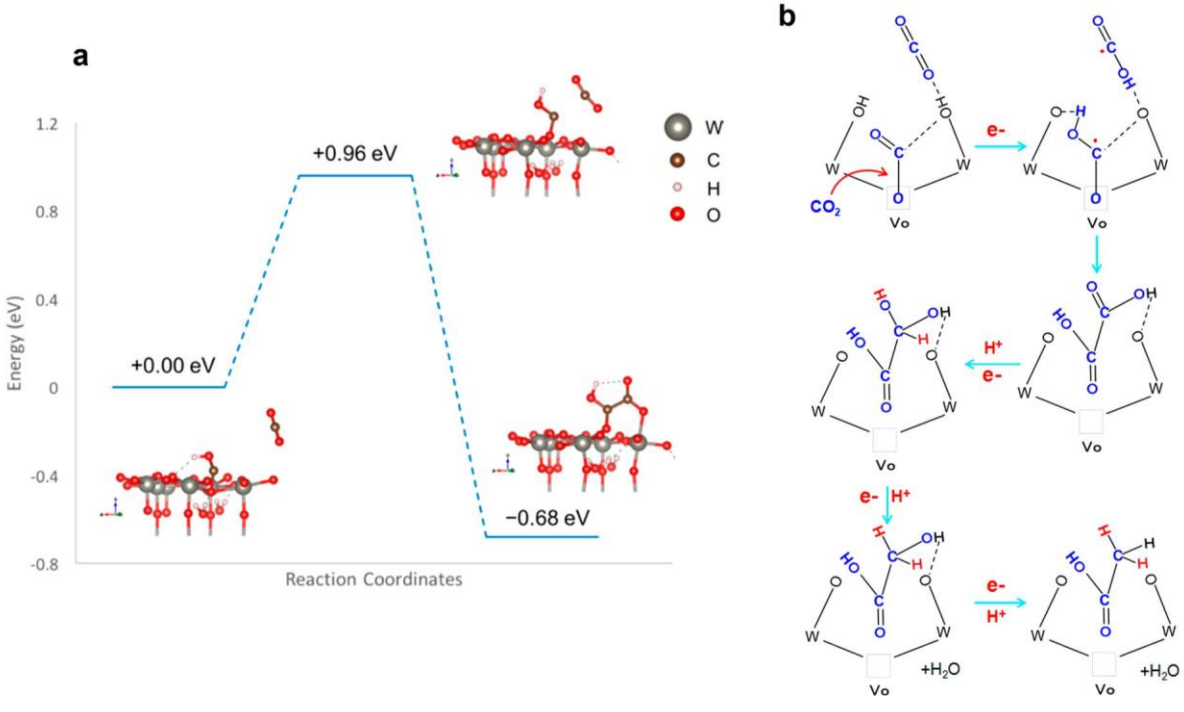

Figure 4. Possible CO_2 activation and hydrogenation process on oxygen-deficient $WO_3 \cdot 0.33H_2O$ {001} surface. (a) Summary of the transition-state analysis and energy changes along the reaction pathway of the C_2 product formation by DFT calculation. The reference energy state is selected to be the oxygen-defective $WO_3 \cdot 0.33H_2O$ {001} surface with one Vo-adsorbed CO_2 and one free CO_2. (b) Schematic illustration of possible reaction pathway for CH_3COOH production.

The above experimental studies have confirmed that the HCO_3 species is a vitally important intermediate for the final acetum production, which is transformed into COOH intermediate under light irradiation. In order to further investigate the hydrogenation mechanism, quantum chemical simulations based on density functional theory (DFT) were conducted on the oxygen-deficient H-WO_3 sample. From the DFT simulation, it was found that protonation of the Vo-adsorbed CO_2 will result in a tightly attached HCO_3 intermediate on the WO_3 surface, because this process further buries the O-atom in a C−O bond to the Vo site and the protonated H-atom can form a hydrogen bond with an adjacent O-atom, as shown in the initial stage of Figure 4a. This result can explain why desorption of HCO_3 species is difficult during TPD measurement. Further calculation found that, once another protonated CO_2 (O C OH) approaches the HCO_3 intermediate under light irradiation, they will react with each other spontaneously and form a C_2 intermediate. During this process, the Vo-adsorbed O-atom in the C−O bond departs from the Vo site because of the formation of an adjacent C−C bond (as shown in the final stage of Figure 4a). This simulation result coincides with the experimental observation that the O-atom did not fill in the Vo site after photocatalytic reaction, making the Vo sustainable. The reaction barrier was calculated by searching the transition state of this reaction using the CI-NEB method, which was found to be 0.96 eV as shown in Figure 4a. This energy barrier is much smaller than the band gap of the $WO_3 \cdot 0.33H_2O$ sample, indicating that the photogenerated electrons are energetic enough to drive the spontaneous reaction for C_2 species production.

At present, there are two main pathways for the photocatalytic CO_2 reduction, depending on whether the hydrogenation or the deoxygenation process is faster.[47,48] Quantum chemical calculations and the in situ DRIFT spectrum revealed that the CO_2 reduction pathway on the as-prepared catalyst might be $CO_2 \rightarrow {}^{\bullet}COOH \rightarrow (COOH)_2 \rightarrow CH_3COOH$ via a hydrogenation process, as shown in Figure 4b. Specifically, upon light irradiation, the unsaturated C O bond in the linear absorbed CO_2, which is coordinated with the surface W-OH group, is attacked by the photogenerated electrons to form one O C OH radical intermediate. Meanwhile, a considerable proportion of the photogenerated electrons are trapped in the middle sub-band of the Vo, and a proton-coupled electron transfer takes place on the Vo-adsorbed HCO bicarbonate species to form another O C OH intermediate radical. The photogenerated electron transfer to Vo can be proved by ESR imaging of the light-irradiated catalyst in CO_2 gas (Figure S14), from which one can see that the single-electron-trapped Vo signal was slightly decreased and shifted to lower magnetic field under light irradiation. If there are not sufficient $H^{\bullet}$ radicals around these newly formed ${}^{\bullet}COOH$ intermediates, the adjacent ${}^{\bullet}COOH$ radicals can form C−C bonds simulta-neously. During this process, the Vo-absorbed O-atom in the O C OH radical gradually departs from the oxygen vacancy (observed from quantum chemical simulation). Different from the deoxygenation process, where the Vo-adsorbed CO_2 usually leaves one oxygen on the Vo to form CO, this hydrogenation process can prevent the deactivation of Vo from oxygen filling. After the C_2 intermediate formed, the Vo-absorbed O-atom completely detached from the Vo site and then formed a HOOC−COOH intermediate. Under light irradiation, proton-coupled electron transfer will proceed on the hydrogen-bond-connected −COOH until the −COOH is reduced to $-CH_3$, and then the acetum product will be formed. This reaction pathway is very similar to the process of electrochemical CO_2 reduction to acetate, which has been proved to proceed via a $CO_2 \rightarrow CO_2^{\bullet-} \rightarrow (COO)_2^{\bullet-} \rightarrow CH_3COO^-$ pathway.[38]

From the above reaction pathway, it can be concluded that the acetum product originates from the reaction of Vo-adsorbed HCO_3 species and the surface OH-adsorbed CO_2. Unlike the previously reported C_1 product, which needs only one active site for reduction of one CO_2 molecule, the acetum product in our experiment is obtained by cooperation of two active sites (Vo and OH) for simultaneous reduction of two CO_2 molecules and then forms a C_2 intermediate $(COOH)_2$. In this process, the Vo-adsorbed CO_2 is easily detached from Vo after the formation of the C−C bond, realizing the sustainable use of the Vo sites. Although CO_2 activation by Vo has been widely reported in previous studies, deactivation of Vo after the photocatalytic reaction has been a general problem. In this study, the collaboration of surface Vo and OH sites to co-activate two CO_2 molecules to form a C_2 intermediate species and suppress the deactivation of Vo is completely new, and it may stimulate other studies on how to increase the selectivity for C_2 species production, and how to maintain the activity of Vo active sites.

CONCLUSION

Ultrathin $WO_3 \cdot 0.33H_2O$ nanotubes with large amounts of sustainable Vo are first explored for photocatalytic CO_2 reduction to CH_3COOH under solar light, showing a high selectivity up to 85%. Systematic experimental studies and quantum chemical calculations revealed an innovative hydro-genation mechanism for CO_2 reduction that involved the collaboration of surface Vo and hydroxyl groups as the main reactive sites responsible for the highly selective CH_3COOH generation. This innovative hydrogenation mechanism protects the surface Vo from O-atom filling during the photocatalytic process. Therefore, the catalytic activity of the oxygen-deficient $WO_3 \cdot 0.33H_2O$ nanotube does not show obvious deactivation even after six repetitive photocatalytic reactions. This study not only puts forward a new strategy for developing high-performance heterogeneous photocatalysts through atomic-scale nanostructure control, but also gives deeper insight into the mechanism of CO_2 activation, which then enables us to establish a strategy to design better photocatalysts.

EXPERIMENTAL SECTION

Preparation. For the H-WO_3 sample, sodium oleate (4.4 mmol) and $Na_2WO_4 \cdot 2H_2O$ (3 mmol) were successively added to distilled water (50 mL). After vigorous stirring for 2 h, the pH value was adjusted to 1 by addition of dilute HNO_3. Before the suspension was transferred to a 100 mL Teflon-lined autoclave, the volume of the precursor suspension was adjusted to 80 mL by adding additional distilled water. The sealed reaction system was heated at 180 °C for 16 h. The system was then allowed to cool down to room temperature. The obtained solid products were collected by centrifugation, washed with absolute ethanol and dilute HNO_3 (10 μL in 20 mL of ethanol) more than three times, and then freeze-dried for further characterization. For comparison, the L-WO_3 sample was prepared without adding sodium oleate in the reaction system. The obtained precursor suspension with a pH value of 1 was sealed in a 100 mL Teflon-lined autoclave filled to 80% of the total volume and then heated at 180 °C for 12 h.

Characterization. The purity and the crystallinity of the as-prepared samples were characterized by powder X-ray diffraction (XRD) on an RINT2500HLR+ X-ray diffractometer (Rigaku, Japan) using Cu Kα radiation while the voltage and electric current were held at 40 kV and 80 mA. Transmission electron microscopy (TEM) analyses were performed by using a JEOL JEM-2100F field emission electron microscope. X-ray photoelectron spectroscopy (XPS) was carried out by irradiating the sample with a 320 μm diameter spot of monochromated aluminum Kα X-rays at 1486.6 eV under ultrahigh vacuum conditions (performed on a PHI5000 Versa Probe system). Diffuse reflectance spectroscopy (DRS) of the sample was performed using a Shimadzu UV-3600 UV−vis−NIR spectrophotometer. The surface-adsorbed organic contaminants were analyzed by solid-state ^{13}C NMR on a Bruker Ascend 400 spectrometer, using 2 g of sample. The in situ DRIFT measurement was performed on a Nicolet 8700 DRIFT spectrometer using a KBr window. Before measurement, the catalyst powder was placed in the cell and evacuated at room temperature for 5 min. Temperature-programmed desorption (TPD) of CO_2 was performed with a commercial instrument (Micotrac Bel, Japan) under vacuum conditions with a quadrupole mass spectrometric detector (Anerva AQA-100). Typically, 30 mg of the sample, placed in a glass tube, was pretreated by a He gas flow at 150 °C for 2 h and then cooled down to 50 °C. The adsorption of CO_2 was performed in a 99.99% CO_2 gas flow (0.1 MPa, 100 mL/min) at 50 °C for 2 h. After evacuation with a vacuum pump at 50 °C for 15 min, the sample was heated from 50 to 500 °C at a rate of 5 °C/min. The TPD signal was recorded by a thermal conductivity detector. Further to identify if the product was formed from CO_2, labeled experiments were done using $^{13}CO_2$, and the products were analyzed with gas chromatography−mass spectrometry (GC-MS) by using a Shimadzu GCMS-QP2010 instrument with a thermal conductivity detector (TCD). Electron spin resonance (ESR) spectra were recorded at 300 K on a Bruker EMX 8/2.7 X-band spectrometer operating under 100 kHz modulation frequency. NMR spectra were acquired on a Bruker AVANCE III 600 spectrometer.

Photocatalytic Test. Photocatalytic CO_2 reduction experiments were performed under a solar simulator (PEC-L11) located approximately 10 cm from the sample. The reaction cell (capacity 600 mL) was made of Pyrex glass with a quartz window on top. Typically, 0.05 g of the as-prepared photocatalyst powder was dispersed in 150 mL deionized water and then stirring under the simulated solar light irradiation. Before illumination, CO_2 (50% in Ar) gas was slowly bubbled through the reaction vessel for 30 min. Then the reaction vessel was sealed and irradiated under the solar simulator. During the photocatalytic tests, the temperature of the reaction vessel was maintained at 4 °C by providing a flow of cooling water. For $^{13}CO_2$ isotopic labeling experiment, pure Ar gas was slowly bubbled through the reaction vessel for 30 min. Next, 200 mL of Ar gas was pumped out from the sealed reaction cell, and 200 mL of $^{13}CO_2$ gas was injected. The concentration of acetic acid and formic acid products in the reactor solution were measured using an ion chromatography system (Dionex, ICS-1000) equipped with an ICE-AS6 column. The concentration of CO was determined with online gas chromatography equipped with a flame ionization detector (Ar carrier) and the catalytic conversion furnace. The amount of H_2O_2 in solution was determined by the titanium sulfate spectrophotometric method via a UV−vis−NIR spectrophotometer (Shimadzu UV-3600).

Electrochemical Measurements. Electrochemical measurements were performed on an IVIUM electrochemical workstation using a standard three-electrode cell with a working electrode, a platinum mesh as counter electrode, and a standard saturated calomel electrode (SCE) in saturated KCl as reference electrode. The working electrodes were prepared by dip-coating. Briefly, 5 mg of photocatalyst was suspended in 0.1 mL of ethanol in the presence of 1% Nafion to produce a slurry, which was then dip-coated onto a 2 cm × 1.5 cm FTO glass electrode and dried at 25 °C.

Computational Methods. Periodic density functional theory (DFT) calculations with spin-polarization were performed using the Vienna Ab Initio Simulation Package (VASP).[49−52] We used the plane wave projector augmented wave (PAW) method for description of the ionic cores. The energy cutoff for the plane wave expansion was 500 eV, and 4×4×4 Γ-centered symmetry-reduced Monkhorst−Pack meshes were used, adequate for geometry optimization. For the CO_2 adsorption energy calculation, the Perdew−Burke−Ernzerhof (PBE) functional form of the generalized gradient approximation was used to describe the non-local exchange and correlation. Convergence is reached if the consecutive energy and force differences are within 10^{-5} eV for electronic iterations and 10^{-2} eV/Å for ionic relaxations.

Three layers of $WO_3 \cdot 0.33H_2O$ were constructed, with the bottom layer fixed. A 10 Å vacuum is applied along the [001] direction to avoid interaction between the periodic images. Dipole corrections and spin-polarization were allowed in all calculations considering the polar nature of the surface. To achieve a better description of the electronic structure of the bulk phase, the band gaps and densities of states of both the ideal and oxygen-deficient $WO_3 \cdot 0.33H_2O$ were calculated using the hybrid B3LYP functional with 20% mixing of the Fock exchange. The oxygen-deficient $WO_3 \cdot 0.33H_2O$ lattice was created by removing one atomic oxygen from a stoichiometric unit cell of $W_3O_9 \cdot H_2O$ so that charge neutrality was maintained. Each of the possible symmetrically unique oxygen vacancy positions was tested. The most energetically stable oxygen defect case was then selected for the band gap and density of states calculations. To evaluate the reaction barrier for the formation of the C_2 product on the $WO_3 \cdot 0.33H_2O$ surface, a transition state search utilizing the climbing image nudged elastic band (CI-NEB) method was carried out. Five intermediate configuration images were linearly interpolated between the stable start and end configurations for the CI-NEB calculations. The two start and end configurations were pre-evaluated to be energetically stable and correspond to the adsorbed and reacted double CO_2 state. During the CI-NEB calculations, the atomic positions were fully relaxed with the lattice constants held fixed.

ASSOCIATED CONTENT

* Supporting Information

Other sample preparation details, additional TEM images, X-ray diffraction patterns (XRD), calculated density of states, solid-state ^{13}C NMR, ^{13}C NMR of intermediate, EIS Nyquist plots, CO_2-TPD, ESR spectra under light, and additional data, including Figures S1− S14 (PDF)

AUTHOR INFORMATION

Corresponding Authors

*songmeisun@i2cner.kyushu-u.ac.jp

*ishihara@cstf.kyushu-u.ac.jp

ORCID

Songmei Sun: 0000-0001-9545-9073

Ji Wu: 0000-0003-3938-8834

Notes

The authors declare no competing financial interest.

ACKNOWLEDGMENTS

This work received financial support from the World Premier International Research Center Initiative (WPI Initiative) on Carbon-Neutral Energy Research (I^2CNER), MEXT (Japan), National Natural Science Foundation of China (No. 21671197), a research grant (No. 16ZR1440800) from Shanghai Science and Technology Commission, and a Grant-in-Aid for Specially Promoted Research (No. 16H06293) from MEXT, Japan. J.W. thanks the funding support from the JSPS, Japan, and the NSF, USA, under the JSPS-NSF Partnerships for International Research and Education (PIRE). The authors would also like to thank Aleksandar Staykov for performing the calculations.

REFERENCES

(1) Halmann, M. Nature 1978, 275, 115−116.

(2) Inoue, T.; Fujishima, A.; Konishi, S.; Honda, K. Nature 1979, 277, 637−638.

(3) Richardson, R. D.; Holland, E. J.; Carpenter, B. K. Nat. Chem. 2011, 3, 301−303.

(4) Zhao, Y.; Chen, G.; Bian, T.; Zhou, C.; Waterhouse, G. I. N.; Wu, L.-Z.; Tung, C.-H.; Smith, L. J.; O'Hare, D.; Zhang, T. Adv. Mater. 2015, 27, 7824−7831.

(5) Liang, L.; Lei, F.; Gao, S.; Sun, Y.; Jiao, X.; Wu, J.; Qamar, S.; Xie, Y. Angew. Chem., Int. Ed. 2015, 54, 13971−13974.

(6) Gao, C.; Meng, Q.; Zhao, K.; Yin, H.; Wang, D.; Guo, J.; Zhao, S.; Chang, L.; He, M.; Li, Q.; Zhao, H.; Huang, X.; Gao, Y.; Tang, Z. Adv. Mater. 2016, 28, 6485−6490.

(7) Ghuman, K. K.; Hoch, L. B.; Szymanski, P.; Loh, J. Y. Y.; Kherani, N. P.; El-Sayed, M. A.; Ozin, G. A.; Singh, C. V. J. Am. Chem. Soc. 2016, 138, 1206−1214.

(8) Seo, H.; Katcher, M. H.; Jamison. Nat. Chem. 2017, 9, 453−456.

(9) Neatu, S.; Macia-Agullo, J. A.; Concepcion, P.; Garcia, H. J. Am. Chem. Soc. 2014, 136, 15969−15976.

(10) Liu, L.; Zhao, H.; Andino, J. M.; Li, Y. ACS Catal. 2012, 2, 1817−1828.

(11) Mori, K.; Yamashita, H.; Anpo, M. RSC Adv. 2012, 2, 3165−3172.

(12) Tu, W.; Zhou, Y.; Liu, Q.; Yan, S.; Bao, S.; Wang, X.; Xiao, M.; Zou, Z. Adv. Funct. Mater. 2013, 23, 1743−1749.

(13) Arai, T.; Sato, S.; Kajino, T.; Morikawa, T. Energy Environ. Sci. 2013, 6, 1274−1282.

(14) Fujiwara, H.; Hosokawa, H.; Murakoshi, K.; Wada, Y.; Yanagida, S. Langmuir 1998, 14, 5154−5159.

(15) Zhou, R.; Guzman, M. I. J. Phys. Chem. C 2014, 118, 11649− 11656.

(16) Liu, Q.; Zhou, Y.; Kou, J.; Chen, X.; Tian, Z.; Gao, J.; Yan, S.; Zou, Z. J. Am. Chem. Soc. 2010, 132, 14385−14387.

(17) Tsai, C. W.; Chen, H. M.; Liu, R. S.; Asakura, K.; Chan, T. S. J. Phys. Chem. C 2011, 115, 10180−10186.

(18) White, J. L.; Baruch, M. F.; Pander, J. E., III; Hu, Y.; Fortmeyer, I. C.; Park, J. E.; Zhang, T.; Liao, K.; Gu, J.; Yan, Y.; Shaw, T. W.; Abelev, E.; Bocarsly, A. B. Chem. Rev. 2015, 115, 12888−12935.

(19) Klepser, B. M.; Bartlett, B. M. J. Am. Chem. Soc. 2014, 136, 1694−1697.

(20) Tomita, O.; Otsubo, T.; Higashi, M.; Ohtani, B.; Abe, R. ACS Catal. 2016, 6, 1134−1144.

(21) Zhang, N.; Li, X.; Ye, H.; Chen, S.; Ju, H.; Liu, D.; Lin, Y.; Ye, W.; Wang, C.; Xu, Q.; Zhu, J.; Song, L.; Jiang, J.; Xiong, Y. J. Am. Chem. Soc. 2016, 138, 8928−8935.

(22) Wang, L.; Wang, Y.; Cheng, Y.; Liu, Z.; Guo, Q.; Ha, M. N.; Zhao, Z. J. Mater. Chem. A 2016, 4, 5314−5322.

(23) Chen, X.; Zhou, Y.; Liu, Q.; Li, Z.; Liu, J.; Zou, Z. ACS Appl. Mater. Interfaces 2012, 4, 3372−3377.

(24) Xie, Y. P.; Liu, G.; Yin, L.; Cheng, H. M. J. Mater. Chem. 2012, 22, 6746−6751.

(25) Liao, L.; Zhang, Q.; Su, Z.; Zhao, Z.; Wang, Y.; Li, Y.; Lu, X.; Wei, D.; Feng, G.; Yu, Q.; Cai, X.; Zhao, J.; Ren, Z.; Fang, H.; Robles-Hernandez, F.; Baldelli, S.; Bao, J. Nat. Nanotechnol. 2014, 9, 69−73.

(26) Zhang, N.; Shi, J.; Mao, S. S.; Guo, L. Chem. Commun. 2014, 50, 2002−2004.

(27) Zhao, J.; Holmes, M. A.; Osterloh, F. E. ACS Nano 2013, 7, 4316−4325.

(28) Sun, S.; Wang, W.; Li, D.; Zhang, L.; Jiang, D. ACS Catal. 2014, 4, 3498−3503.

(29) Sun, Y. F.; Liu, Q.; Gao, S.; Cheng, H.; Lei, F.; Sun, Z.; Jiang, Y.; Su, H.; Wei, S.; Xie, Y. Nat. Commun. 2013, 4, 2899.

(30) Zhang, W.; Wang, L.; Liu, H.; Hao, Y.; Li, H.; Khan, M. U.; Zeng, J. Nano Lett. 2017, 17, 788−793.

(31) Khan, M. U.; Wang, L.; Liu, Z.; Gao, Z.; Wang, S.; Li, H.; Zhang, W.; Wang, M.; Wang, Z.; Ma, C.; Zeng, J. Angew. Chem., Int. Ed. 2016, 55, 9548−9552.

(32) Xie, S.; Wang, Y.; Zhang, Q.; Deng, W.; Wang, Y. ACS Catal. 2014, 4, 3644−3653.

(33) Zhai, Q.; Xie, S.; Fan, W.; Zhang, Q.; Wang, Y.; Deng, W.; Wang, Y. Angew. Chem., Int. Ed. 2013, 52, 5776−5779.

(34) Cheng, H.; Wen, M.; Ma, X.; Kuwahara, Y.; Mori, K.; Dai, Y.; Huang, B.; Yamashita, H. J. Am. Chem. Soc. 2016, 138, 9316−9324.
(35) Yin, H.; Kuwahara, Y.; Mori, K.; Cheng, H.; Wen, M.; Huo, Y.; Yamashita, H. J. Phys. Chem. C 2017, 121, 23531−23540.
(36) Ji, Y.; Luo, Y. J. Am. Chem. Soc. 2016, 138, 15896−15902.
(37) Xi, G.; Ouyang, S.; Li, P.; Ye, J.; Ma, Q.; Su, N.; Bai, H.; Wang, C. Angew. Chem., Int. Ed. 2012, 51, 2395−2399.
(38) Liu, Y.; Chen, S.; Quan, X.; Yu, H. J. Am. Chem. Soc. 2015, 137, 11631−11636.
(39) Xu, P.; Milstein, T. J.; Mallouk, T. E. ACS Appl. Mater. Interfaces 2016, 8, 11539−11547.
(40) Matsumoto, Y. J. Solid State Chem. 1996, 126, 227−234.
(41) Philipp, R.; Fujimoto, K. J. Phys. Chem. 1992, 96, 9035−9038.
(42) Yang, C. C.; Yu, Y. H.; van der Linden, B.; Wu, J. C. S.; Mul, G. J. Am. Chem. Soc. 2010, 132, 8398−8406.
(43) Su, W. G.; Zhang, J.; Feng, Z.; Chen, T.; Ying, P.; Li, C. J. Phys. Chem. C 2008, 112, 7710−7716.
(44) Nie, X.; Esopi, M. R.; Janik, M. J.; Asthagiri, A. Angew. Chem., Int. Ed. 2013, 52, 2459−2462.
(45) Xiao, H.; Cheng, T.; Goddard, W. A., III J. Am. Chem. Soc. 2017, 139, 130−136.
(46) Lin, X.; Yoon, Y.; Petrik, N. G.; Li, Z.; Wang, Z.-T.; Glezakou, V.-A.; Kay, B. D.; Lyubinetsky, I.; Kimmel, G. A.; Rousseau, R.; Dohnalek, Z. J. Phys. Chem. C 2012, 116, 26322−26334.
(47) Liu, L.; Zhao, C.; Li, Y. J. Phys. Chem. C 2012, 116, 7904−7912.
(48) Habisreutinger, S. N.; Schmidt-Mende, L.; Stolarczyk, J. K. Angew. Chem., Int. Ed. 2013, 52, 7372−7408.
(49) Kresse, G.; Hafner, J. Phys. Rev. B: Condens. Matter Mater. Phys. 1993, 47, 558−561.
(50) Kresse, G.; Furthmuller, J. Comput. Mater. Sci. 1996, 6, 15−50.
(51) Kresse, G.; Furthmüller, J. Phys. Rev. B: Condens. Matter Mater. Phys. 1996, 54, 11169−11186.
(52) Kresse, G.; Joubert, D. Phys. Rev. B: Condens. Matter Mater. Phys. 1999, 59, 1758−1775.